Front. Chem. Sci. Eng. 2021, 15(6): 1537–1549
https://doi.org/10.1007/s11705-021-2094-2

RESEARCH ARTICLE

Graphene-like *h*-BN supported polyhedral NiS_2/NiS nanocrystals with excellent photocatalytic performance for removing rhodamine B and Cr(VI)

Wei Wang[1], Linlin Song[1], Huoli Zhang (✉)[1], Guanghui Zhang[1], Jianliang Cao (✉)[1,2]

1 College of Chemistry and Chemical Engineering, Henan Key Laboratory of Coal Green Conversion, Henan Polytechnic University, Jiaozuo 454000, China
2 State Collaborative Innovation Center of Coal Work Safety and Clean-efficiency Utilization, Henan Polytechnic University, Jiaozuo 454000, China

Abstract Human health is deteriorating due to the effluent containing heavy metal ions and organic dyes. Hence, photoreduction of Cr(VI) to Cr(III) and degradation of rhodamine B (RhB) using a novel photocatalyst is particularly important. In this work, *h*-BN/NiS_2/NiS composites were prepared via a simple solvothermal method and a double Z-scheme heterojunction was constructed for efficiently removing RhB and Cr(VI). The 7 wt-% *h*-BN/NiS_2/NiS composites were characterized via a larger specific surface area (15.12 $m^2 \cdot g^{-1}$), stronger light absorption capacity, excellent chemical stability, and high yield of electrons and holes. The experimental result indicated that the photoreduction efficiency of the 7 wt-% *h*-BN/NiS_2/NiS photocatalyst achieved 98.5% for Cr(VI) after 120 min, which was about 3 times higher than that of NiS_2/NiS (34%). However, the removal rate of RhB by the 7 wt-% *h*-BN/NiS_2/NiS photocatalyst reached 80%. This is due to the double Z-scheme heterojunction formed between NiS_2/NiS and *h*-BN, which improved the charge separation efficiency and transmission efficiency. Besides, the influence of diverse photogenerated electron and hole scavengers upon the photoreduction of Cr(VI) was studied, the results indicated that graphene-like *h*-BN promoted transportation of photoinduced charges on the surface of the *h*-BN/NiS_2/NiS photocatalyst via the interfacial effects.

Keywords graphene-like *h*-BN, *h*-BN/NiS_2/NiS composites, photocatalysis, Cr(VI) reduction, degradation of RhB

Received April 15, 2021; accepted July 12, 2021

E-mails: zhanghuoli@hpu.edu.cn (Zhang H),
caojianliang@hpu.edu.cn (Cao J)

1 Introduction

To date, increasing attention has been paid to environmental problems and human health all over the world [1]. A heavy metal ion or an organic dye is extensively present in the effluent from textile, electroplating, ceramic, machinery, and mining manufacturing industries, which is a major threat to human health [2–4]. The best method of eliminating Cr(VI) ions would be to convert Cr(VI) to low poisonous Cr(III) ions, meanwhile, rhodamine B (RhB) could be oxidized to small molecules (CO_2 and H_2O). Nowadays, many new solutions have been researched and applied to waste water treatment, such as spontaneous reduction, electroreduction, and photoreduction [5]. In contrast, photocatalytic reduction has been in the spotlight as a prospective way owing to its sustainability and eco-friendly nature.

Until now, precious metal-based photocatalysts have been regarded as highly efficient catalysts and can reach high energy conversion efficiency [6]. However, the defects and high cost impede in the way of large-scale application of precious metal-based materials. To change this unfavorable situation, much research has been done and some metal sulfides have been widely employed as highly efficient photocatalysts to improve the photocatalytic efficiency as well as lower the product costs [7,8]. In particular, hybridized bimetallic sulfides have better photocatalytic performance than monometallic sulfides [9,10]. When two or more metal species were combined, more active sites could be provided and the electrochemical reaction was promoted. Kuang et al. [11] systematically investigated the MoS_2-NiS_2/NGF composites for effective water splitting. MoS_2-NiS_2/NGF afforded ample active sites and multiple paths during transmission of electrons, which benefited from the synergistic effect of NGF and

bimetallic sulfides. Luo et al. [12] prepared CF/MoS_2/Bi_2S_3 cloth in a controlled manner via a hydrothermal-solvothermal two-step method. MoS_2/Bi_2S_3 decorated carbon-fiber cloth exhibited a higher photocurrent and photocatalytic activity for efficiently degrading various types of flowing wastewater. Most importantly, bimetallic sulfides are to form the heterointerfaces, which are able to modify the surface properties of particles and enhance the stability and photocatalytic performances, which have been reported previously [13,14].

In order to further improve the photocatalytic performance, a recently used effective way is to incorporate transition-metal sulfides with graphene-like boron nitride. Recently, boron nitride with a diversified sheet structure has been successfully synthesized by various methods, including mechanical method [15], chemical vapor deposition [16], and liquid phase exfoliation [17]. It has been proved to be a prospective support for different composites because of its diversified sheet structure, higher surface area, chemical resistance, excellent thermal stability, and nontoxicity [18]. The high porosity of *h*-BN can effectively increase the accessible superficial area of loaded catalysts and supply abundant active sites. Due to its unique electronic structure, and *h*-BN also has inherent negative charges, which make it a good material for hole receptors and for promoting the hole/electron carrier separation [19,20]. In addition, other methods have been developed for synthesizing composites, such as assisted sol-gel method, electrospinning, impregnation, and in-situ precipitation. However, the solvothermal method offers more advantages, including simple preparation, environment friendly, and low cost.

Based on the above studies, in the present study, a designed solvothermal method for fabrication of the ternary catalyst of *h*-BN nanosheet supported NiS_2 and NiS nanocrystals was introduced. Of particular interest to the work, the *h*-BN/NiS_2/NiS composite was able to fully combine the advantages of both *h*-BN and bimetallic sulfides, constructing a double Z-scheme heterojunction and offering more active sites. The *h*-BN/NiS_2/NiS composite showed a higher photocatalytic performance than the other counterparts. Because of the synergistic effect, strong interactions existed in the composite, which achieved a higher activity and cycling stability for eliminating Cr(VI) and RhB pollution. The result can offer a novel reference for exploring a rational design of highly efficient photocatalysts.

2 Experimental

2.1 Reagents

All the reagents were of analytical grade, containing $Ni(NO_3)_2 \cdot 6H_2O$, sulfur powder (S), ethylene glycol (EG), polyvinylpyrrolidone (PVP K-30000), ethanol (C_2H_6O), RhB, $K_2Cr_2O_7$, $KBrO_3$, edetate disodium (EDTA-2Na), isopropanol (IPA), $AgNO_3$, 1,4-benzoquinone (BQ), Na_2SO_4, and Nafion solution (Sigma-Aldrich).

2.2 Synthesis of the *h*-BN/NiS_2/NiS composite

Zhang et al. [21] have reported the controllable preparation method of graphene-like *h*-BN. *h*-BN/NiS_2/NiS composites were successfully synthesized by a solvothermal method. In the synthesis approach, moderate amounts of *h*-BN powders were firstly dispersed in 80 mL of EG under sonication for 60 min. Then, 0.349 g $Ni(NO_3)_2 \cdot 6H_2O$ and 0.064 g S power were dispersed into 60 mL of the above mixed solution by stirring for 20 min. Afterwards, 0.12 g PVP was added to the above mixture and stirred for 40 min, the as-obtained mixture was transferred to a 100 mL Teflon-lined stainless-steel reactor for solvothermal reaction and kept at 200 °C for 12 h. Finally, the resultant black mixture was isolated by centrifugation and washed several times with distilled water and absolute ethanol, and finally, it was dried at 60 °C for 12 h. Using the above method, 3, 5, 7 and 10 wt-% *h*-BN/NiS_2/NiS photocatalysts were prepared in turn, and the detailed synthesis method is illustrated in Scheme 1.

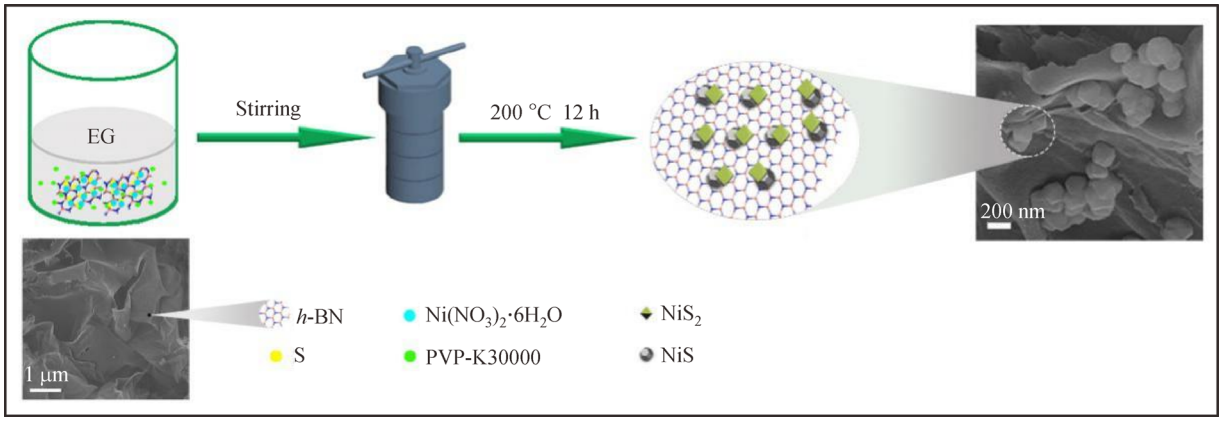

Scheme 1 Schematic illustration of *h*-BN/NiS_2/NiS photocatalysts synthesis.

2.3 Characterization

Phase structures of the sample were analyzed by a Bruker-AXS D8 X-ray diffraction (XRD) system. The XRD patterns with Cu-Kα as the irradiation source and a scanning speed of $5°\cdot min^{-1}$ were recorded in the range of 2θ = 10°–80°. The morphological characteristics of the samples were observed via scanning electron microscopy (SEM, Quanta™250 FEG), transmission electron microscope (TEM, JEOL/JEM 2100 F) at 200 kV. The element chemical information was observed via PHI 5600 X-ray photoelectron spectroscopy (XPS). Ultra-violet-visible (UV-vis) diffuse reflectance spectroscopy (DRS, UV-240) was used to evaluate the visible-light absorption capacity. The photocurrent response and electrochemical impedance spectroscopy (EIS) measurements were performed on the CHI-650E electrochemical workstation (Chenhua, China).

2.4 Photocatalytic performance evaluation

Photocatalytic performances of the as-prepared samples were investigated by eliminating Cr(VI) ($K_2Cr_2O_7$) and RhB. Firstly, a 20 mg *h*-BN/NiS_2/NiS composite was added to 100 mL of 10 $mg\cdot L^{-1}$ $K_2Cr_2O_7$ or 100 mL of 10 $mg\cdot L^{-1}$ RhB during this experiment. Before illumination, the mixture solution was stirred in darkness for some time to achieve the absorption-desorption equilibrium. After that, the lighting apparatus, a 300 W Xenon lamp, was used for simulating sunlight. Then, a mixture of 10 mL was taken out from the suspension every 30 min and centrifuged at 8000 $r\cdot min^{-1}$ for 5 min to remove the photocatalyst. Finally, the concentration of Cr(VI) or RhB was measured in accordance with the absorption peaks at 352 or 554 nm by the UV-vis spectrophotometer.

2.5 Photoelectrochemical measurement

Photoelectrochemical performance of the sample was measured by a CHI-650E electrochemical workstation (Chenhua, China) using Ag/AgCl and Pt wire as reference and counter electrodes, respectively. Moreover, the light source was a 300 W Xenon lamp and 0.5 $mol\cdot L^{-1}$ Na_2SO_4 was used as the electrolyte solution. During preparation of the working electrode, the sample was added into 1 mL ethanol and ultrasonicated for 20 min to form a slurry. Then, Nafion as an adhesive, 5 μL adhesive, and 20 μL slurry were dripped on the indium tin oxide glass with a 0.5 cm^2 conductor. Finally, a whole working electrode was successfully obtained.

3 Results and discussion

For analyzing the crystal phase structure of the undoped and *h*-BN supported NiS_2/NiS samples, the XRD pattern has been shown in Fig. 1. For the polyhedral NiS_2/NiS nanocrystals, the major cubic phase NiS_2 (JCPDS file No. 73-0574) together with a little hexagonal phase NiS (JCPDS file No. 75-0613) could be observed, and there were no other impurities. In addition, two broad diffraction peaks of *h*-BN with a layered structure located at about 26.5° and 42.3° were detected, which were in accordance with the (002) and (100) crystal planes of pure *h*-BN (JCPD file no.34-0421) [22]. However, in terms of the 7 wt-% *h*-BN/NiS_2/NiS composite, no characteristic peaks of *h*-BN could be found; this may be a result of the great dispersion property, the weak diffraction intensity, and low content of *h*-BN [23,24].

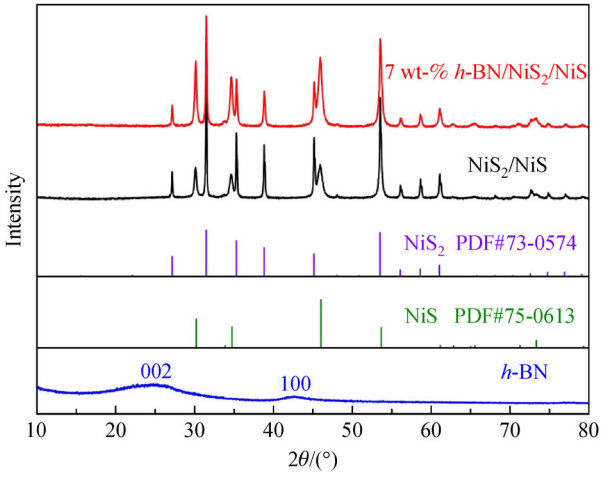

Fig. 1 XRD patterns of different samples.

Figure 2 shows the morphology of *h*-BN, NiS_2/NiS, and 7 wt-% *h*-BN/NiS_2/NiS composite. In Figs. 2(a) and 2(d), 2D *h*-BN as an outstanding photocatalytic substrate material exhibited a peculiar graphene-like layer structure. In addition, the form of 2D graphene-like *h*-BN nanosheets appeared to curl during high temperature calcination under nitrogen atmosphere (Fig. 2(d)). Figures 2(b) and 2(e) show the uniform morphology of NiS_2/NiS nanocrystals with a size of about 200 nm. And, we can confirm that the polyhedral NiS_2/NiS nanocrystals could successfully obtained by a facile solvothermal method. Besides, two different polyhedrons (NiS_2 and NiS) were also observed in Figs. 2(b) and 2(e), which was in line with the XRD result. In Figs. 2(c) and 2(f), a large number of NiS_2/NiS heterojunctions were evenly distributed on the surface of *h*-BN by the solvothermal method, which could effectively increase the more active sites in *h*-BN/NiS_2/NiS. The intimate interfaces between NiS_2/NiS and *h*-BN nanosheets might have promoted electrons transfer for enhancing the photocatalytic performance. Moreover, in Fig. 2(g), Ni, S, B, and N elements and the basic shape of the polyhedral NiS_2/NiS nanocrystal were clearly observed on energy dispersive spectrometer (EDS) elemental mapping; thus, indicating that *h*-BN nanosheets successfully supported the polyhedral NiS_2/NiS nanocrystal.

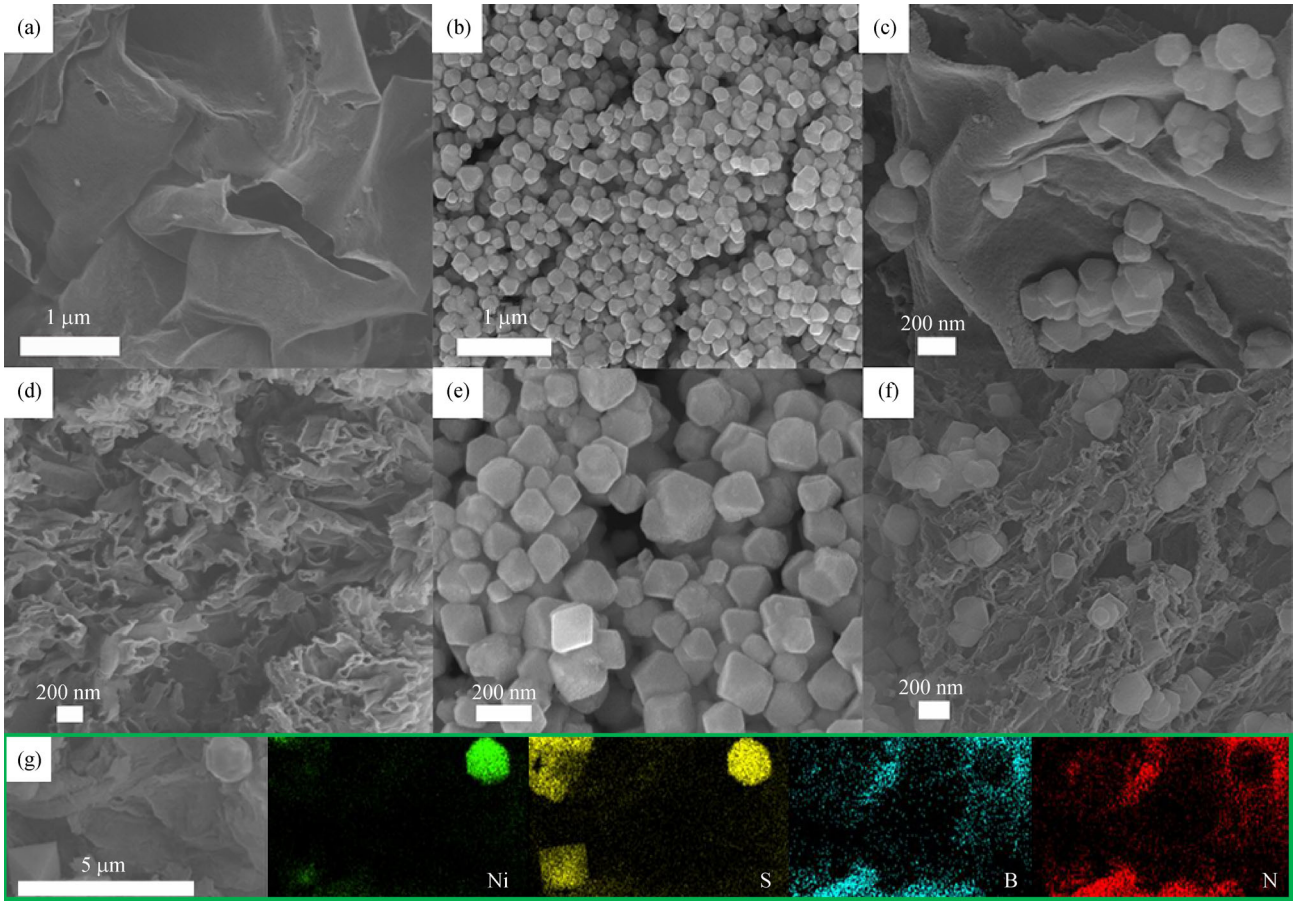

Fig. 2 SEM images of (a, d) *h*-BN, (b, e) NiS_2/NiS, (c, f) 7 wt-% *h*-BN/NiS_2/NiS; (g) EDS elemental mapping of 7 wt-% *h*-BN/NiS_2/NiS for Ni, S, B, and N.

The microstructure of 7 wt-% *h*-BN/NiS_2/NiS was observed by TEM images and EDS spectrum in Fig. 3. In Figs. 3(a,b), the graphene-like *h*-BN nanosheets could be obviously found on the surface of polyhedral NiS_2 and NiS nanocrystals. Among them, the crystal size of the polyhedral NiS_2 and NiS was approximately 200 nm. As shown in Fig. 3(c), the distinct graphene-like *h*-BN nanosheet with a lattice distance of 0.33 nm was in agree with the (102) plane [25]. Besides, the interplanar pitch of the (200) plane of NiS_2 was 0.284 nm [26]. But, Fig. 3(d) corresponded to the red square in Fig. 3(c), the lattice pitch of 0.198 nm was consistent with the (102) plane of NiS [27]. These results were in accordance with the analysis outcome of XRD, proving the existence of *h*-BN, polyhedral NiS_2 and NiS nanocrystals. Figures 3(c,d) display the existence of a tight heterojunction interface between polyhedral NiS_2/NiS nanocrystals and graphene-like *h*-BN nanosheets. In addition, the EDS spectrum confirmed that the prepared 7 wt-% *h*-BN/NiS_2/NiS composite contained Ni, S, B, and N, and no other impurity elements (Fig. 3(e)). The 7 wt-% *h*-BN/NiS_2/NiS composite was the ternary structure composite photocatalyst, and the heterojunction interfaces provided fast electron transport channel, which effectively improved the photocatalytic activity of the photocatalyst.

As shown in Fig. 4, the XPS measurement was investigated for 7 wt-% *h*-BN/NiS_2/NiS to analyze the corresponding chemical states of elements. It can be seen from Fig. 4(a) that the survey spectra of the 7 wt-% *h*-BN/NiS_2/NiS composite proved the presence of Ni, S, B, and N, which was in accordance with the EDS analysis. Figure 4(b) shows the XPS spectrum of B 1s and the peak value 190.7 eV could be clearly discovered, which can be attributed to B-N bonding. In Fig. 4(c), the major N 1s peak at 398.4 eV was attributed to N^{3-} in *h*-BN. For the obtained NiS_2/NiS sample, Fig. 4(d) displays the high-resolution XPS spectra of Ni 2p, two peaks located at 856.3 and 876.4 eV belonging with $2p_{3/2}$ and $2p_{1/2}$ of Ni^{2+}. The peaks of 853.7 and 873.6 eV were ascribed to $2p_{3/2}$ and $2p_{1/2}$ of Ni^{3+}. Besides, satellite peaks confirmed the existence of the Ni^{2+} oxidation state. The surface slight oxidation of NiS_2/NiS led to the appearance of Ni^{3+}, which was in accordance with previous research [28,29]. Two strong peaks of S 2p at 161.7 and 162.4 eV were observed in Fig. 4(e), which corresponded to S $2p_{1/2}$ and S $2p_{3/2}$ of Ni-S bonding, while the peak at 163.6 eV was attributed to

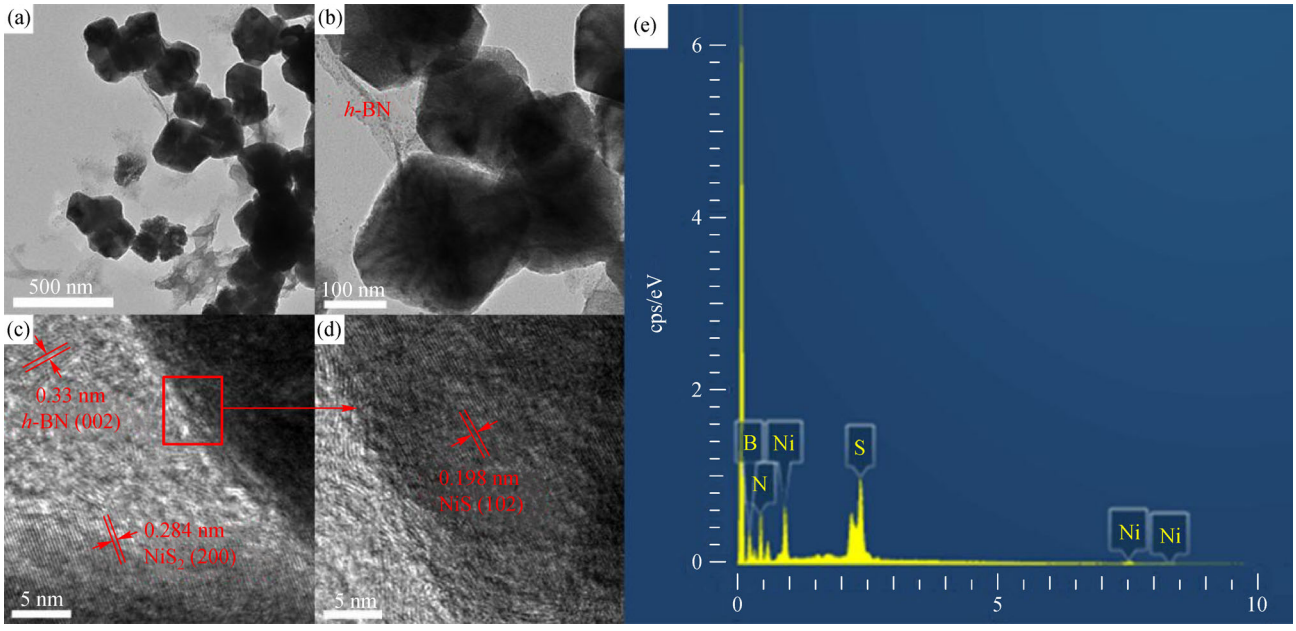

Fig. 3 (a, b) TEM and (c, d) high-resolution TEM images of 7 wt-% *h*-BN/NiS_2/NiS photocatalyst; (e) EDS spectrum of 7 wt-% *h*-BN/NiS_2/NiS photocatalyst.

divalent sulfide ions (S_2^{2-}) [29]. In addition, a small peak at 168.8 eV was assigned to the sulfates with high oxidation state, which resulted from the oxidation of S^{2-} during sample preparation [30]. More importantly, in Figs. 4(d,e), compared with binding energies of NiS_2/NiS, the Ni^{3+} $2p_{3/2}$ (853.7 eV), Ni^{2+} $2p_{3/2}$ (856.5 eV), Ni^{3+} $2p_{1/2}$ (874.1 eV), Ni^{2+} $2p_{1/2}$ (877.1 eV) and S^{2-} $2p_{1/2}$ (161.7 eV), S^{2-} $2p_{3/2}$ (162.4 eV), S_2^{2-} 2p (163.6 eV) in the 7 wt-% *h*-BN/NiS_2/NiS showed a positive shift, which was related to the electron cloud density of Ni and S. However, the change in binding energy was negatively related to the direction of electron migration in the composites, implying that the electrons migrated to *h*-BN nanosheets from the NiS_2/NiS surface [31]. The XPS results proved that the double Z-scheme heterostructure of the 7 wt-% *h*-BN/NiS_2/NiS composite had formed, which effectively accelerated the transport and separation of electrons.

The nitrogen adsorption-desorption isotherms (Fig. 5) of *h*-BN, NiS_2/NiS, and 7 wt-% *h*-BN/NiS_2/NiS were characteristic of type-IV curves with a hysteresis loop, which indicated the presence of a mesoporous structure [32]. The insets in Figs. 5(a–c) show the distribution of pore size, and the pore size of *h*-BN, NiS_2/NiS, and 7 wt-% *h*-BN/NiS_2/NiS displayed mainly ranged from 0.98–3.97, 1.69–6.51, and 1.61–5.20 nm, respectively. In Figs. 5(b,c), the specific surface area of 7 wt-% *h*-BN/NiS_2/NiS (15.12 $m^2 \cdot g^{-1}$) was larger than that of NiS_2/NiS (10.82 $m^2 \cdot g^{-1}$), which can be attributed to the introduction of *h*-BN, and the Brunner-Emmett-Teller (BET) surface area of *h*-BN (Fig. 5(a)) was 1571.78 $m^2 \cdot g^{-1}$; thus, *h*-BN as a promising support can supply abundant active sites for effectively improving the photocatalytic performance. Besides, according to the Barrett-Joyner-Halenda method, the corresponding cumulative pore volumes were calculated by the desorption branch curve of the N_2 adsorption–desorption isotherms and it showed cumulative pore volumes of 0.995, 0.017 and 0.024 $cm^3 \cdot g^{-1}$, respectively.

The photocatalytic performances of NiS_2/NiS and *h*-BN/NiS_2/NiS were investigated via Cr(VI) reduction and degradation of RhB (Fig. 6). In Fig. 6(a), a small amount of *h*-BN supported NiS_2/NiS nanocrystals could improve the photocatalytic activity. The BET surface area of *h*-BN was 1571.78 $m^2 \cdot g^{-1}$; thus, 7 wt-% *h*-BN/NiS_2/NiS with a BET surface area of 15.12 $m^2 \cdot g^{-1}$ was larger than NiS_2/NiS (10.82 $m^2 \cdot g^{-1}$). The introduction of *h*-BN provided large specific surface area for NiS_2/NiS composite; thus, adsorption of Cr(VI) by *h*-BN/NiS_2/NiS was higher than that by NiS_2/NiS after 60 min in a dark room. At darkness, the 7 wt-% *h*-BN/NiS_2/NiS photocatalyst was added, and after 30 min, the adsorption of RhB reached 10.75%. After irradiation for 120 min, only 34.0 wt-% of Cr(VI) was removed by NiS_2/NiS, but 7, 5 and 3 wt-% *h*-BN/NiS_2/NiS photocatalysts could eliminate about 98.5%, 92.6%, and 43.3% of Cr(VI), respectively. The reason for this occurrence may be that the double Z-scheme heterostructure promoted the separation efficiency of the photogenerated carriers. However, the photocatalytic performance of 10 wt-% *h*-BN/NiS_2/NiS was lower than that of the 7 wt-% *h*-BN/NiS_2/NiS photocatalyst, which may be due to excess *h*-BN covering the photocatalytic active sites on the NiS_2/NiS nanocrystal surface. For Cr(VI) reduction, the absorption peaks at 372 nm are illustrated using the 7 wt-% *h*-BN/NiS_2/NiS photocatalyst during a 30 min interval (Fig. 6(b)). With irradiation time prolongation, the

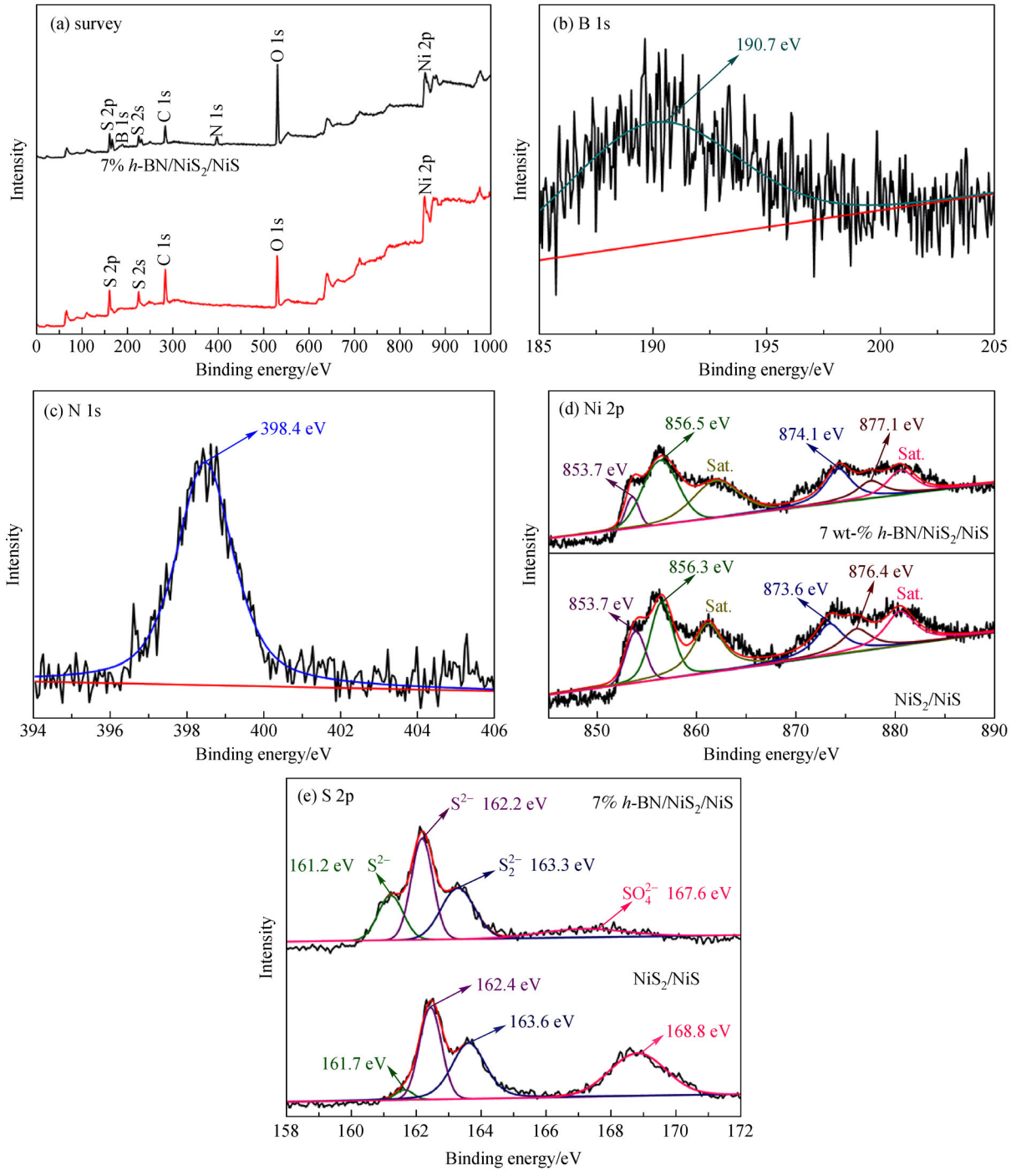

Fig. 4 XPS spectra of 7 wt-% *h*-BN/NiS_2/NiS (a) survey spectra, (b) B 1s, (c) N 1s, (d) Ni 2p, (e) S 2p.

absorption peaks were gradually decreased and they disappeared after 120 min, indicating that Cr(VI) could be converted to Cr(III) by the 7 wt-% *h*-BN/NiS_2/NiS photocatalyst.

Figure 6(c) shows that the experimental results for reduction Cr(VI) by NiS_2/NiS and 7 wt-% *h*-BN/NiS_2/NiS conformed to the pseudo-first-order dynamics plot. The dynamics model was calculated by the following formula $-\ln(C/C_0) = k \cdot t$ [33], where k is the reaction rate constant, t is the photocatalytic reaction time, C_0 and C are concentrations of the $K_2Cr_2O_7$ solution before illumination and at time t. In Fig. 6(d), the reaction rate constant for Cr (VI) reduction by NiS_2/NiS nanocrystals, 3, 5, 7 and 10 wt-% *h*-BN/NiS_2/NiS composites were 0.0029, 0.0074, 0.0218, 0.0284 and 0.0096 min^{-1}, respectively. Apparently, the photoreduction rate of the 7 wt-% *h*-BN/NiS_2/NiS

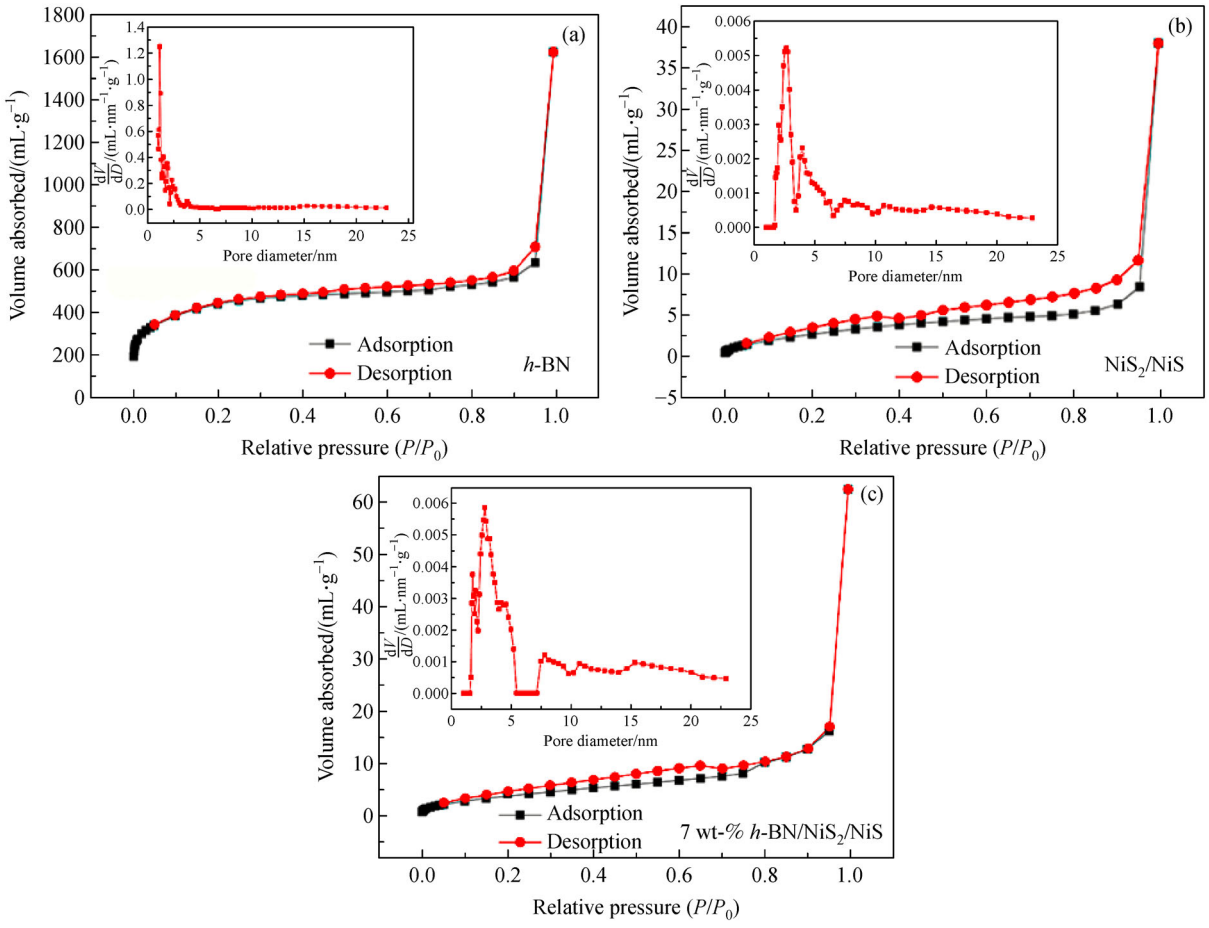

Fig. 5 N_2 adsorption-desorption isotherms and pore size distribution curves (inset) of (a) *h*-BN, (b) NiS_2/NiS, and (c) 7 wt-% *h*-BN/NiS_2/NiS.

photocatalyst for Cr(VI) was the highest. For degradation of RhB (10 mg·L^{-1}), the RhB adsorption and photocatalytic performance were also tested (Fig. 6(e)). At darkness, after 30 min, the 7 wt-% *h*-BN/NiS_2/NiS photocatalyst was added, the RhB solution achieved the adsorption-desorption equilibrium and the adsorption of RhB reached 10.75%. After irradiation for 180 min, the degradation efficiency of RhB reached 80%, and RhB had been oxidized by superoxide radicals, hydroxyl radicals, and holes to many small molecules (H_2O and CO_2). In terms of the four time photocatalytic recycling test, the 7 wt-% *h*-BN/NiS_2/NiS composite still had good stability in reducing Cr(VI) (Fig. 6(f)).

In Table 1, the photocatalytic activity of the other NiS_x-based composites is exhibited for comparison with *h*-BN/NiS_2/NiS, and it showed that *h*-BN/NiS_2/NiS had an outstanding photoreduction performance.

In Fig. 7, Fig. 7(a) exhibits the UV-vis DRS of different samples in the region between 200 and 700 nm. It may be seen that the graphene-like *h*-BN displayed absorption characteristic in the ultraviolet range of 200–300 nm due to the wide band gap of *h*-BN. NiS_2/NiS nanocrystals showed a stronger light absorption performance in the region of 200–700 nm, which is beneficial for photocatalysis [42,43]. After the introduction of *h*-BN, the optical absorption characteristic of the 7 wt-% *h*-BN/NiS_2/NiS composite was greatly enhanced; thus, showing that it could be used as an effective photocatalyst. However, the light absorption capability of the 7 wt-% *h*-BN/NiS_2/NiS composite was slightly lower than that of NiS_2/NiS nanocrystals, which may be attributed to white color of *h*-BN [44]. The DRS result indicated that there was a strong interaction between NiS_2/NiS and *h*-BN, favoring photocatalytic reactions.

In Fig. 7(b), the Cr(VI) removal mechanism was testified by the addition of 1 mmol $KBrO_3$ as the trapping agent of photoelectrons. Compared with the no scavenger group, Cr(VI) reduction was suppressed by adding $KBrO_3$ [45]. The addition of $KBrO_3$ considerably decreased the photoreduction rate from 97.1% to 40.4% after 2 h, proving that 7 wt-% *h*-BN/NiS_2/NiS sample produced electrons. Further, transient photocurrent responses (Fig. 7(c)) were performed by 400 s on-off cycles under light irradiation. With the introduction of *h*-BN,

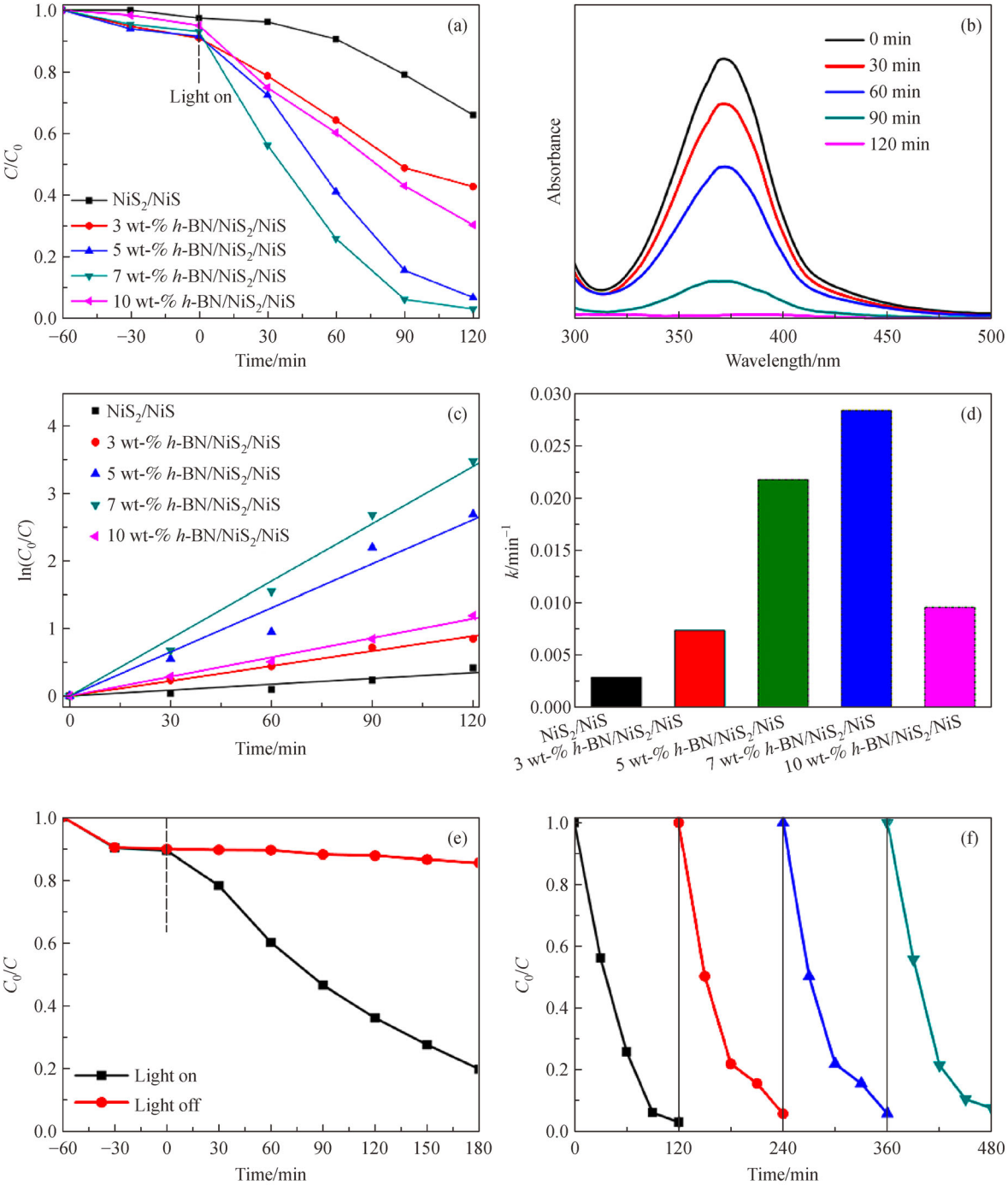

Fig. 6 (a) Photoreduction efficiency of Cr(VI) (10 mg·L^{-1}) with adding different photocatalysts under light irradiation; (b) UV-vis absorption spectra of Cr(VI) under different time using 7 wt-% *h*-BN/NiS_2/NiS photocatalyst; (c) kinetics curves of Cr(VI) reduction; (d) rate constant k; (e) degradation of RhB (10 mg·L^{-1}) with adding 7 wt-% *h*-BN/NiS_2/NiS composites; (f) recycling test of photoreduction Cr(VI).

h-BN/NiS_2/NiS composite samples displayed a higher photocurrent intensity compared with NiS_2/NiS, and it can be conjectured that electrons could be more easily transferred between the *h*-BN and NiS_2/NiS interface, and the 7 wt-% *h*-BN/NiS_2/NiS composites displayed the highest photo-current density. It was demonstrated that a double Z-scheme heterojunction was formed between NiS_2/NiS and *h*-BN, which improved the charge separation efficiency and facilitated the effective separation of electron-hole pairs. As shown in Fig. 7(d), 7 wt-%

Table 1 Comparison of the photocatalytic performances in the present work and the previously reported NiS_x-based composites

Catalyst	Pollutant	Light source	Removal	Time/min	Ref.
NiS_2-rGO	Congo red	Simulated sunlight	97.03%	40	[34]
NiS/$LaFeO_3$	Methyl orange	Simulated sunlight	90.9%	120	[35]
α-NiS/Bi_2O_3	Tramadol	250 W Xe lamp	94%	180	[36]
NiS_2/g-C_3N_4	Ciprofloxacin	350 W Xe lamp	65%	210	[37]
$BiVO_4$/NiS/Au	Tetracycline	300 W Xe lamp	82%	25	[38]
$NiGaO_4$/NiS_2/WO_3	NO_2^-	Simulated sunlight	87.03%	240	[39]
NiS/$BiVO_4$	Methyl orange	300 W Xe lamp	95.6%	90	[40]
NiS/BiOBr	RhB	450 W Xe lamp	99.5%	50	[41]
NiS_2 (111)/rGO	Cr(VI)	1100 W Xe lamp	97%	150	[8]
h-BN/NiS_2/NiS	Cr(VI)	300 W Xe lamp	98.5%	120	This work

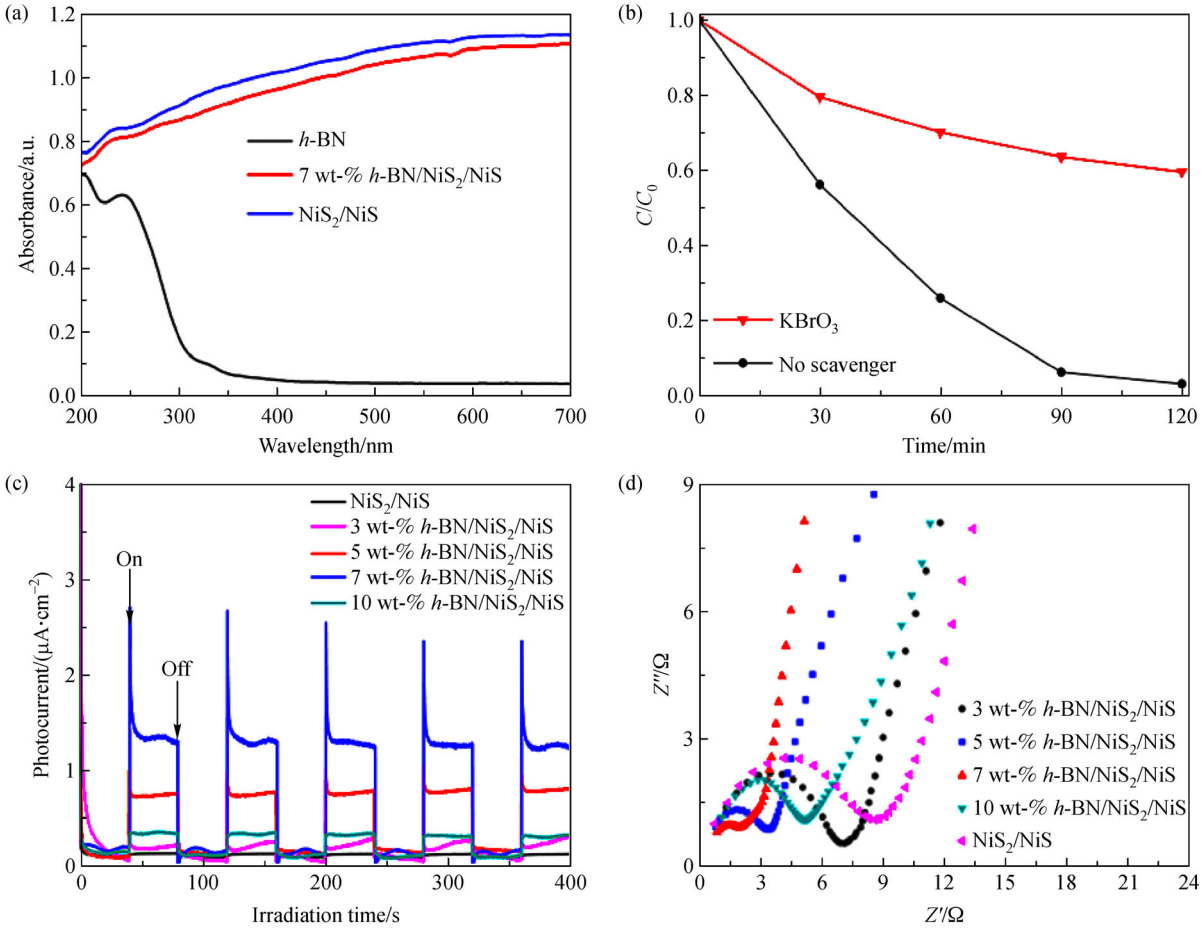

Fig. 7 (a) UV-vis DRS and (b) photoreduction Cr(VI) with different scavenger of 7 wt-% *h*-BN/NiS_2/NiS; (c) transient photocurrent responses and (d) EIS of NiS_2/NiS and 3, 5, 7 and 10 wt-% *h*-BN/NiS_2/NiS samples.

h-BN/NiS_2/NiS photocatalysts exhibited a smallest semicircle radius on an EIS Nyquist plot than other photocatalysts, suggesting that *h*-BN reduced electron transfer resistance as a typical 2D graphene-like material. Therefore, the test result was also consistent with improvement in the Cr(VI) photoreduction rate and degradation efficiency of RhB.

Photoluminescence (PL) spectra analysis was performed

to further study the separation efficiency of electron-hole pairs with a Xe lamp as an illuminant (Fig. 8). Figures 8(a, b) display the PL spectra of NiS_2/NiS and *h*-BN/NiS_2/NiS composite samples under the excitation of 357 nm, and NiS_2/NiS had the strongest emission spectrum with the peak located at about 435 nm, manifesting the highest recombination rate of electron-hole pairs. However, the 7 wt-% *h*-BN/NiS_2/NiS composite showed the weakest PL emission intensity compared with NiS_2/NiS nanocrystals, which meant that the existence of *h*-BN could decrease the recombination rate of electron-hole pairs [46]. The result indicated the double Z-scheme electron transfer pathway from NiS_2/NiS to *h*-BN [47], which was conducive to improving the catalytic property of the photocatalyst. These phenomena were in accordance with the analysis outcome of EIS, UV-vis DRS, and transient photocurrent responses. Therefore, the *h*-BN/NiS_2/NiS photocatalyst was effective for degradation of RhB and reduction of Cr(VI).

With respect to the above experiments and discussion, in Fig. 9, a reasonable mechanism is illustrated for eliminating Cr (VI) and RhB. First, DRS analysis indicated that 7 wt-% *h*-BN/NiS_2/NiS displayed a wider absorption range compared with the NiS_2/NiS nanocrystals in harvesting light. Second, graphene-like *h*-BN improved the photocatalytic performance of NiS_2/NiS nanocrystals, and this can be attributed to the interfacial charge transfer along the double Z-scheme route. According to the literature, the NiS_2 had a conduction band (CB) potential of 0.89 V (*vs.* NHE) and a valence band (VB) potential of 1.19 V

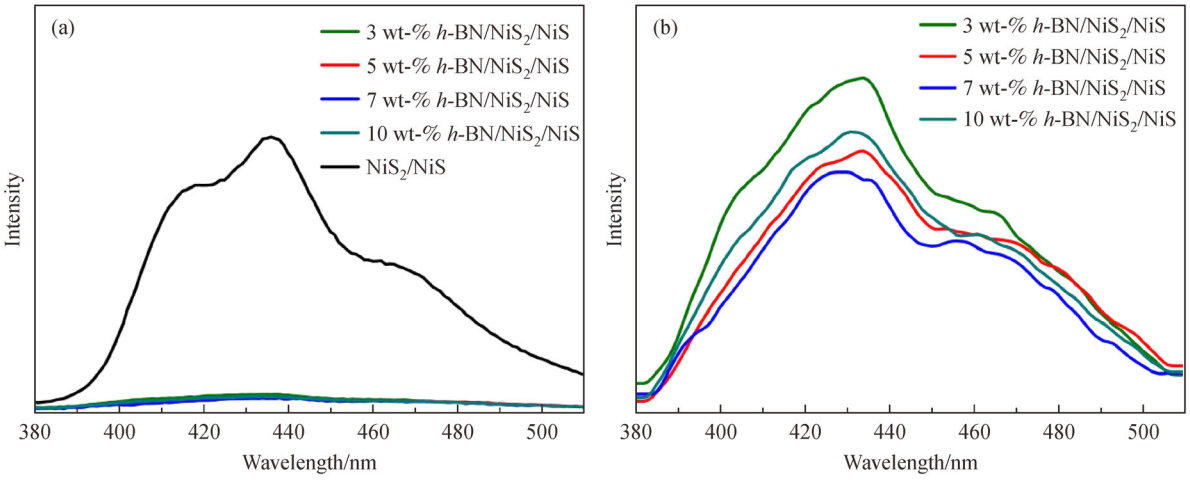

Fig. 8 PL spectra of (a) the as-prepared *h*-BN/NiS_2/NiS and NiS_2/NiS, and (b) *h*-BN/NiS_2/NiS photocatalysts with different contents of *h*-BN.

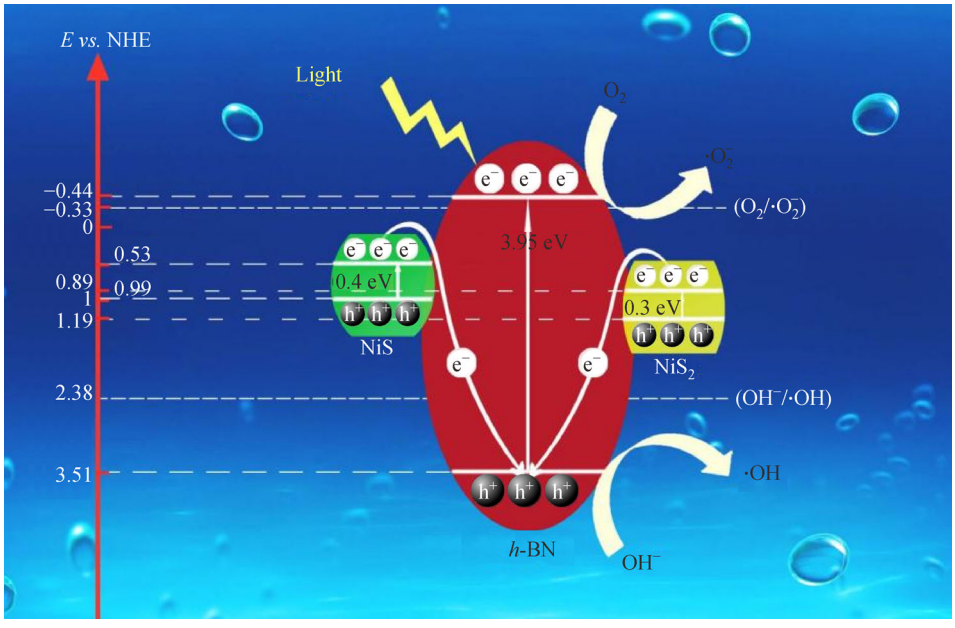

Fig. 9 Schematic mechanism of 7 wt-% *h*-BN/NiS_2/NiS photocatalyst.

(*vs.* NHE), the CB and VB values of NiS were 0.53 and 0.99 V in potential *vs.* NHE, respectively. Therefore, the band gaps of NiS and NiS_2 were 0.4 and 0.3 eV, respectively [37,48]. For *h*-BN, the CB potential of *h*-BN (–0.44 eV) was a negativity greater than –0.33 eV in terms of the O_2/•O_2^- reduction potential, and the VB potential of *h*-BN (3.51 eV) was greater than the oxidation potential of OH^-/•OH (2.38 eV). Further, the actual valence/conduction band energies of samples were tested (Fig. S1 and Fig. S2, cf. Electronic Supplementary Material). When the 7 wt-% *h*-BN/NiS_2/NiS photocatalyst was irradiated, the photoinduced electrons in NiS and NiS_2 were excited and rapidly transferred from VB to CB. The electrons in the CB of NiS_2 and NiS recombined with some of the holes in the VB of *h*-BN, forming a double Z-scheme heterojunction. The remaining holes could combine with OH^- on the surface of *h*-BN to form •OH (E^0(OH^-/•OH) = 2.38 eV), while adsorbed O_2 was reduced to •O_2^- (E^0 (O_2/•O_2^-) = –0.33 eV) by electrons in the VB of *h*-BN [49]. Then, the RhB could also be oxidized by •O_2^- and •OH to many small molecules (H_2O and CO_2). It has been demonstrated that the double Z-scheme heterostructure between NiS_2/NiS nanocrystals and *h*-BN effectively separated electrons in the CB of *h*-BN. Therefore, the graphene-like *h*-BN supported NiS_2/NiS nanocrystals can provide more photogenerated electrons and holes for enhancing the photocatalytic activity in removing RhB and Cr(VI).

4 Conclusions

The graphene-like *h*-BN/NiS_2/NiS ternary composite was fabricated to utilize the solvothermal method, and it displayed a superior photocatalytic performance for eliminating Cr(VI) and RhB. The double Z-scheme heterojunction formed between NiS_2/NiS and *h*-BN facilitated rapid separation of electron-hole pairs as well as effective electron migration. In addition, because of the double Z-scheme heterojunction, the 7 wt-% *h*-BN/NiS_2/NiS photocatalyst achieved 98.5% for Cr(VI) after 120 min, which was about 3 times higher than that of NiS_2/NiS (34%). Meanwhile, the 7 wt-% *h*-BN/NiS_2/NiS photocatalyst also exhibited excellent photocatalytic performance for removing RhB, and it also had excellent stability. This study offers a viable reference to develop a stably effective and BN-based bimetallic sulfide photocatalytic material for purifying wastewater.

Acknowledgements This study was financially supported by Program for Science & Technology Innovative Research Team in the University of Henan Province (Grant No. 21IRTSTHN006), Program for Science & Technology Innovation Talents in Universities of Henan Province (Grant No. 19HASTIT042), Key scientific and technological project in Henan Province (Grant No. 212102210179), Program for Innovative Research Team of Henan Polytechnic University (Grant Nos. T2018-2, T2019-1).

Electronic Supplementary Material Supplementary material is available in the online version of this article at https://dx.doi.org/10.1007/s11705-021-2094-2 and is accessible for authorized users.

References

1. Kumaravel V, Mathew S, Bartlett J, Pillai S C. Photocatalytic hydrogen production using metal doped TiO_2: a review of recent advances. Applied Catalysis B: Environmental, 2019, 244: 1021–1064
2. Yang D, Zou X, Sun Y, Tong Z, Jiang Z. Fabrication of three-dimensional porous La-doped $SrTiO_3$ microspheres with enhanced visible light catalytic activity for Cr(VI) reduction. Frontiers of Chemical Science and Engineering, 2018, 12(3): 440–449
3. Alharbi N S, Hu B, Hayat T, Rabah S O, Alsaedi A, Zhuang L, Wang X. Efficient elimination of environmental pollutants through sorption-reduction and photocatalytic degradation using nanomaterials. Frontiers of Chemical Science and Engineering, 2020, 14(6): 1124–1135
4. Li D, Li J, Jin Q, Ren Z, Sun Y, Zhang R, Zhai Y, Liu Y. Photocatalytic reduction of Cr (VI) on nano-sized red phosphorus under visible light irradiation. Journal of Colloid and Interface Science, 2019, 537: 256–261
5. Du X, Yi X, Wang P, Deng J, Wang C. Enhanced photocatalytic Cr (VI) reduction and diclofenac sodium degradation under simulated sunlight irradiation over MIL-100(Fe)/g-C_3N_4 heterojunctions. Chinese Journal of Catalysis, 2019, 40(1): 70–79
6. Qiu J, Zhang X F, Zhang X, Feng Y, Li Y, Yang L, Lu H, Yao J. Constructing $Cd_{0.5}Zn_{0.5}S$@ZIF-8 nanocomposites through self-assembly strategy to enhance Cr(VI) photocatalytic reduction. Journal of Hazardous Materials, 2018, 349: 234–241
7. Wu J, Liu B, Ren Z, Ni M, Li C, Gong Y, Qin W, Huang Y, Sun C Q, Liu X. CuS/RGO hybrid photocatalyst for full solar spectrum photoreduction from UV/Vis to near-infrared light. Journal of Colloid and Interface Science, 2018, 517: 80–85
8. Liang Y, Yang Y, Xu K, Yu T, Yang Q, Shi P, Yuan C. Crystal facets engineering and rGO hybridizing for synergistic enhancement of photocatalytic activity of nickel disulfide. Journal of Hazardous Materials, 2020, 384: 121402
9. Li L, Wu J, Liu B, Liu X, Li C, Gong Y, Huang Y, Pan L. NiS sheets modified CdS/reduced graphene oxide composite for efficient visible light photocatalytic hydrogen evolution. Catalysis Today, 2018, 315: 110–116
10. Yu X, Du R, Li B, Zhang Y, Liu H, Qu J, An X. Biomolecule-assisted self-assembly of CdS/MoS_2/graphene hollow spheres as high-efficiency photocatalysts for hydrogen evolution without noble metals. Applied Catalysis B: Environmental, 2016, 182: 504–512
11. Kuang P, He M, Zou H, Yu J, Fan K. 0D/3D MoS_2-NiS_2/N-doped graphene foam composite for efficient overall water splitting. Applied Catalysis B: Environmental, 2019, 254: 15–25
12. Luo L, Shen X, Song L, Zhang Y, Zhu B, Liu J, Chen Q, Chen Z, Zhang L. MoS_2/Bi_2S_3 heterojunctions-decorated carbon-fiber cloth as flexible and filter-membrane-shaped photocatalyst for the efficient degradation of flowing wastewater. Journal of Alloys and Compounds, 2019, 779: 599–608
13. Yang Y, Zhang K, Lin H, Li X, Chan H C, Yang L, Gao Q. MoS_2-

Ni_3S_2 heteronanorods as efficient and stable bifunctional electrocatalysts for overall water splitting. ACS Catalysis, 2017, 7(4): 2357–2366

14. Luo S, Dong S, Lu C, Yu C, Ou Y, Luo L, Sun J, Sun J. Rational and green synthesis of novel two-dimensional WS_2/MoS_2 heterojunction via direct exfoliation in ethanol-water targeting advanced visible-light-responsive photocatalytic performance. Journal of Colloid and Interface Science, 2018, 513: 389–399
15. Streletskii A N, Permenov D G, Bokhonov B B, Kolbanev I V, Leonov A V, Berestetskaya I V, Streletzky K A. Destruction, amorphization and reactivity of nano-BN under ball milling. Journal of Alloys and Compounds, 2009, 483(1-2): 313–316
16. Song L, Ci L L, Lu H, Sorokin P B, Jin C, Ni J, Kvashnin A G, Kvashnin D G, Lou J, Yakobson B I, Ajayan P M. Large scale growth and characterization of atomic hexagonal boron nitride layers. Nano Letters, 2010, 10(8): 3209–3215
17. Marsh K L, Souliman M, Kaner R B. Co-solvent exfoliation and suspension of hexagonal boron nitride. Chemical Communications, 2015, 51(1): 187–190
18. Zhou C, Lai C, Zhang C, Zeng G, Huang D, Cheng M, Hu L, Xiong W, Chen M, Wang J, Yang Y, Jiang L. Semiconductor/boron nitride composites: synthesis, properties, and photocatalysis applications. Applied Catalysis B: Environmental, 2018, 238: 6–18
19. Li J, Lei N, Guo L, Song Q, Liang Z. Constructing h-BN/Bi_2WO_6 quantum dot hybrid with fast charge separation and enhanced photoelectrochemical performance by using *h*-BN for hole transfer. ChemElectroChem, 2018, 5(2): 300–308
20. Liu D, Zhang M, Xie W, Sun L, Chen Y, Lei W. Porous BN/TiO_2 hybrid nanosheets as highly efficient visible-light-driven photocatalysts. Applied Catalysis B: Environmental, 2017, 207: 72–78
21. Zhang R, Wang J, Han P. Highly efficient photocatalysts of Pt/BN/CdS constructed by using the Pt as the electron acceptor and the BN as the holes transfer for H_2-production. Journal of Alloys and Compounds, 2015, 637: 483–488
22. Song L, Jia H, Zhang H, Cao J. Graphene-like *h*-BN/CdS 2D/3D heterostructure composite as an efficient photocatalyst for rapid removing rhodamine B and Cr(VI) in water. Ceramics International, 2020, 46(15): 24674–24681
23. Ding S, Mao D, Yang S, Wang F, Meng L, Han M, He H, Sun C, Xu B. Graphene-analogue *h*-BN coupled Bi-rich $Bi_4O_5Br_2$ layered microspheres for enhanced visible-light photocatalytic activity and mechanism insight. Applied Catalysis B: Environmental, 2017, 210: 386–399
24. Xu H, Wu Z, Ding M, Gao X. Microwave-assisted synthesis of flower-like BN/BiOCl composites for photocatalytic Cr(VI) reduction upon visible-light irradiation. Materials & Design, 2017, 114: 129–138
25. Chen T, Zhang Q, Xie Z, Tan C, Chen P, Zeng Y, Wang F, Liu H, Liu Y, Liu G, Lv W. Carbon nitride modified hexagonal boron nitride interface as highly efficient blue LED light-driven photocatalyst. Applied Catalysis B: Environmental, 2018, 238: 410–421
26. Jourshabani M, Shariatinia Z, Achari G, Langford C H, Badiei A. Facile synthesis of NiS_2 nanoparticles ingrained in a sulfur-doped carbon nitride framework with enhanced visible light photocatalytic activity: two functional roles of thiourea. Journal of Materials Chemistry. A, Materials for Energy and Sustainability, 2018, 6(27): 13448–13466
27. Zhang R, Lu C, Shi Z, Liu T, Zhai T, Zhou W. Hexagonal phase NiS octahedrons co-modified by 0D-, 1D-, and 2D carbon materials for high-performance supercapacitor. Electrochimica Acta, 2019, 311: 83–91
28. Liu P, Li J, Lu Y, Xiang B. Facile synthesis of NiS_2 nanowires and its efficient electrocatalytic performance for hydrogen evolution reaction. International Journal of Hydrogen Energy, 2018, 43(1): 72–77
29. Lu M, Gao N, Zhang X J, Wang G S. Reduced graphene oxide decorated with octahedral NiS_2/NiS nanocrystals: facile synthesis and tunable high frequency attenuation. RSC Advances, 2019, 9 (10): 5550–5556
30. Lv J, Cheng Y, Liu W, Quan B, Liang X, Ji G, Du Y. Achieving better impedance matching by a sulfurization method through converting Ni into NiS/Ni_3S_4 composites. Journal of Materials Chemistry. C, Materials for Optical and Electronic Devices, 2018, 6 (7): 1822–1828
31. Bai X, Du Y, Hu X, He Y, He C, Liu E, Fan J. Synergy removal of Cr (VI) and organic pollutants over RP-MoS_2/rGO photocatalyst. Applied Catalysis B: Environmental, 2018, 239: 204–213
32. Xue D, Wang P, Zhang Z, Wang Y. Enhanced methane sensing property of flower-like SnO_2 doped by Pt nanoparticles: a combined experimental and first-principle study. Sensors and Actuators. B, Chemical, 2019, 296: 126710
33. Chen Y, Li J F, Liao P Y, Zeng Y S, Wang Z, Liu Z Q. Cascaded electron transition in $CuWO_4$/CdS/CDs heterostructure accelerating charge separation towards enhanced photocatalytic activity. Chinese Chemical Letters, 2020, 31(6): 1516–1519
34. Borthakur P, Das M R. Hydrothermal assisted decoration of NiS_2 and CoS nanoparticles on the reduced graphene oxide nanosheets for sunlight driven photocatalytic degradation of azo dye: effect of background electrolyte and surface charge. Journal of Colloid and Interface Science, 2018, 516: 342–354
35. Wang X T, Li Y, Zhang X Q, Li J F, Li X, Wang C W. Design and fabrication of NiS/$LaFeO_3$ heterostructures for high efficient photodegradation of organic dyes. Applied Surface Science, 2020, 504: 144363
36. Majhi D, Samal P K, Das K, Gouda S K, Bhoi Y P, Mishra B G. α-NiS/Bi_2O_3 nanocomposites for enhanced photocatalytic degradation of tramadol. ACS Applied Nano Materials, 2018, 2(1): 395–407
37. Zhu C, Jiang Z, Chen L, Qian K, Xie J. L-Cysteine-assisted synthesis of hierarchical NiS_2 hollow spheres supported carbon nitride as photocatalysts with enhanced lifetime. Nanotechnology, 2017, 28(11): 115708
38. Zhang G C, Zhong J, Xu M, Yang Y, Li Y, Fang Z, Tang S, Yuan D, Wen B, Gu J. Ternary $BiVO_4$/NiS/Au nanocomposites with efficient charge separations for enhanced visible light photocatalytic performance. Chemical Engineering Journal, 2019, 375: 122093
39. Ma X, Wang G, Wang C, Li S, Wang J, Song Y. NiS_2 as trapezoid conductive channel modified ternary Z-scheme photocatalyst system, $NiGa_2O_4/NiS_2/WO_3$, for highly photocatalytic simultaneous conversions of NO_2^- and SO_3^{2-}. Chemical Engineering Journal, 2018, 350: 364–377
40. Li Y, Li X, Wang X T, Jian L J, Abdallah N I M, Dong X F, Wang C W. P-n heterostructured design of decahedral NiS/$BiVO_4$ with

efficient charge separation for enhanced photodegradation of organic dyes. Colloids and Surfaces. A, Physicochemical and Engineering Aspects, 2021, 608: 125565

41. Hu M, Yan A, Cui Q, Huang F, Li D, Li F, Huang J, Qiang Y. NiS/BiOBr hybrids with retarded carrier recombination and enhanced visible-light-driven photocatalytic activity. Journal of Materials Science, 2019, 55(10): 4265–4278
42. Pan J, Wang B, Dong Z, Zhao C, Jiang Z, Song C, Wang J, Zheng Y, Li C. The 2D RGO-NiS_2 dual co-catalyst synergistic modified g-C_3N_4 aerogel towards enhanced photocatalytic hydrogen production. International Journal of Hydrogen Energy, 2019, 44(36): 19942–19952
43. Li L, Wu J, Liu B, Liu X, Li C, Gong Y, Huang Y, Pan L. NiS sheets modified CdS/reduced graphene oxide composite for efficient visible light photocatalytic hydrogen evolution. Catalysis Today, 2018, 315: 110–116
44. Gu J, Yan J, Chen Z, Ji H, Song Y, Fan Y, Xu H, Li H. Construction and preparation of novel 2D metal-free few-layer BN modified graphene-like g-C_3N_4 with enhanced photocatalytic performance. Dalton Transactions (Cambridge, England), 2017, 46(34): 11250–11258
45. Liu Z, Wang Q, Rong W, Jin R, Cui Y, Gao S. CTAB assisted hydrothermal preparation of Bi_2WO_6-WO_3 nanosheets on TiO_2 nanotube arrays for photoelectrocatalytic applications. Separation and Purification Technology, 2018, 200: 191–197
46. Wu Y, Wang H, Tu W, Liu Y, Wu S, Tan Y Z, Chew J W. Construction of hierarchical 2D-2D $Zn_3In_2S_6$/fluorinated polymeric carbon nitride nanosheets photocatalyst for boosting photocatalytic degradation and hydrogen production performance. Applied Catalysis B: Environmental, 2018, 233: 58–69
47. Ye L, Wen Z, Li Z, Huang H. Hierarchical architectured ternary nanostructures photocatalysts with $In(OH)_3$ nanocube on $ZnIn_2S_4$/NiS nanosheets for photocatalytic hydrogen evolution. Solar RRL, 2020, 4(8): 2000027
48. Ma X, Wang C, Wang G, Li G, Li S, Wang J, Song Y. Three narrow band-gap semiconductors modified Z-scheme photocatalysts, Er^{3+}: $Y_3Al_5O_{12}$@$NiGa_2O_4$/(NiS, CoS_2 or MoS_2)/$Bi_2Sn_2O_7$, for enhanced solar-light photocatalytic conversions of nitrite and sulfite. Journal of Industrial and Engineering Chemistry, 2018, 66: 141–157
49. He S, Xiao K, Chen X Z, Li T, Ouyang T, Wang Z, Guo M L, Liu Z Q. Enhanced photoelectrocatalytic activity of direct Z-scheme porous amorphous carbon nitride/manganese dioxide nanorod arrays. Journal of Colloid and Interface Science, 2019, 557: 644–654